
DATA-DRIVEN VIRTUAL TEST-BED OF THE BLOWN POWDER DIRECTED ENERGY DEPOSITION PROCESS

Michael Juhasz

Lawrence Livermore National Laboratory
Livermore, CA
juhasz1@llnl.gov

Eric Chin

Lawrence Livermore National Laboratory
Livermore, CA
chin23@llnl.gov

Youngsoo Choi

Lawrence Livermore National Laboratory
Livermore, CA
choi15@llnl.gov

Joseph T. McKeown

Lawrence Livermore National Laboratory
Livermore, CA
mckeown3@llnl.gov

Saad Khairallah

Lawrence Livermore National Laboratory
Livermore, CA
khairallah1@llnl.gov

September 11, 2024

ABSTRACT

Digital twins in manufacturing serve as a crucial bridge between the industrial age and the digital age, offering immense value. Current additive manufacturing processes are able to generate vast amounts of in-process data, which, when effectively ingested, can be transformed into insightful decisions. Data-driven methods from reduced order modeling and system identification are particularly promising in managing this data deluge. This study focuses on Laser Powder Directed Energy Deposition (LP-DED) equipped with in-situ process measurements to develop a compact virtual test-bed. This test-bed can accurately ingest arbitrary process inputs and report in-process observables as outputs. This virtual test-bed is derived using Dynamic Mode Decomposition with Control (DMDc) and is coupled with uncertainty quantification techniques to ensure robust predictions.

1 Introduction

Additive manufacturing, a relatively young set of practices, has garnered significant attention and promise over the past few decades. This promise lies in its ability to enable designers and engineers to create better, lighter, and stronger products. However, unlike traditional manufacturing methods, additive manufacturing introduces new challenges, particularly significant uncertainties between input process parameters and the final product [33, 39]. These uncertainties can range from variations in material performance to shape defects and geometrical non-conformance [24, 38]. While these issues affect different additive manufacturing techniques to varying degrees, this study focuses on directed energy deposition.

Directed energy deposition (DED), also known as laser metal deposition (LMD), direct metal deposition (DMD), and colloquially as LENS®, is one of the seven archetypal forms of additive manufacturing [13, 7, 1]. In DED, metal powder is delivered to a substrate where a heat source, typically a laser, simultaneously induces melting, thereby depositing material. The preferred machine arrangement in DED is still under debate, but for this study, we use a laser heat source with the powder feedstock delivered coaxially to the laser beam through an annulus nozzle.

To better understand the link between input process parameters and the final product, on-machine monitoring (OMM) is employed during the process. OMM involves using sensors to record the in-process state. Common sensors measure the size, temperature, and light emission intensity of the molten pool, but these represent only a small subset of available sensor modalities [15, 11]. In this study, the OMM suite on the DED machine includes coaxial measurement of melt pool size and temperature, as well as an off-axis camera that measures the working distance between the nozzle and melt pool centroid. Additional measurements are summarized in *Table 1*. While having this in-process information is valuable, our focus is on managing and generating impactful insights from the data that can be applied to previously unseen input/actuation.

On-Machine Monitoring (OMM) Capability		
Process Monitoring Sensors (states)	Process Inputs	Environment Monitoring Sensors
Melt Pool Size (mm)	Laser Commanded Power (Watts)	Enclosure Temperature (C)
Melt Pool Temperature (C)	Laser Spot Size Diameter (mm)	Enclosure H2O (ppm)
Real-time Working Distance (mm)	Scan Rate (mm/min)	Enclosure Pressure (mbar)
Powder Flow (Counts)	X Position (mm)	Enclosure O2 (ppm)
Process Camera Centroid X (Px)	Y Position (mm)	
Process Camera Centroid Y (Py)	Z Position (mm)	
Laser Power Feedback (Watts)	Powder Hopper Disc Speed (RPM)	
	Powder Hopper Carrier Gas (l/min)	
	Shield Gas (l/min)	
	Current Layer (#)	
	Infill Flag (Bool)	
	Contour Flag (Bool)	
	Set Working Distance (mm)	
	Program Slice Resolution (mm)	
	Post Layer Delay (s)	

Table 1: Table of the OMM capability of the DED machine used. Note that derived quantities such as laser energy density (J/mm^2) or heading angle (deg) are also available in these datasets as part of the OMM capability.

System models are indispensable tools in engineering, science, and various other fields, providing a structured approach to understanding, predicting, and optimizing the behavior of complex systems. These models form the foundation of what are known as digital twins [8]. Digital twins are virtual replicas of physical systems that are used to simulate, analyze, and optimize real-world processes. We have adopted the term "virtual test-bed" to specifically highlight not only the replication of processes but also the extension to unseen inputs and actuation. Hartmann *et al.* have summarized the current state of digital twins/system models in the context of additive manufacturing (AM), noting that achieving an accurate system model with relatively low computational cost remains a significant milestone yet to be reached [18].

These models can be broadly categorized into physical (white-box), hybrid (gray-box), and data-driven (black-box), each with its unique advantages and applications. In DED, both Mukherjee and Khairallah *et al.* stressed the need for accurate, physical simulation models [30, 25]. Other physical models have also been presented by Ertay *et al.* and Weisz-Patrault [12, 42]. To contrast, Gaikwad *et al.* demonstrated a hybrid, physical and data-driven model that combined physical simulation with in-situ sensor data and showed that the predictive capacity increased through this combination [15].

Our work presented here is a purely data-driven model which relies entirely on empirical data to make predictions without any explicit knowledge of the system's internal workings. These models use algorithms to identify patterns and relationships within the data, making them highly versatile and capable of handling complex, nonlinear systems. They do, however, require large amounts of high-quality data for training and can sometimes lack interpretability, making it challenging to understand how predictions are made. Within this data-driven paradigm, two key sub-branches are system identification and reduced order modeling (ROM). Among these techniques, dynamic mode decomposition (DMD) introduced by Schmid and its variants, such as dynamic mode decomposition with control (DMDc), have gained prominence for their ability to extract low-order models from high-dimensional data [34, 31].

ROMs aim to simplify complex systems by reducing the number of degrees of freedom while retaining essential dynamic characteristics. Techniques such as proper orthogonal decomposition (POD) and DMD are commonly used [3, 34]. POD identifies the most energetic modes in a system, while DMD decomposes the system into modes that capture both spatial and temporal dynamics. Autoregressive models, which predict future states based on past observations, are also widely used. System identification involves developing mathematical models of dynamic systems based on

measured data [28]. Techniques in this area include output-error methods, which minimize the difference between observed and predicted outputs, and Hammerstein-Wiener models, which combine linear dynamic models with static nonlinearities. Subspace identification methods use state-space representations to identify system dynamics from input-output data. Other traditional methods, such as the Eigensystem Realization Algorithm (ERA) and Observer Kalman Filter Identification (OKID), use connections between measurements and observability and controllability matrices from control theory [22, 23]. However, these methods focus on single impulse-response measurements, which, in an additive manufacturing context, would require averaging across many derived system matrices to achieve the same consensus as DMD/DMDc.

In recent years, machine learning techniques have become integral to system identification and ROM. Neural networks, which can approximate complex nonlinear functions, are increasingly used to model system dynamics. Long Short-Term Memory (LSTM) networks, a type of recurrent neural network, are particularly effective for time-series prediction due to their ability to capture long-term dependencies. AutoEncoders, which learn efficient representations of data, are used for dimensionality reduction and feature extraction [16]. Notable recent advancements in the field include Sparse Identification of Nonlinear Dynamics (SINDy) and Latent Space Dynamics Identification (LaSDI) [4, 14]. SINDy identifies governing equations of a system by promoting sparsity in the model, making it interpretable and efficient. LaSDI leverages latent space representations to identify dynamics, enabling the modeling of complex systems with reduced computational cost.

In this work, we employ DMDc, a derivative of DMD. DMDc extends the DMD framework by incorporating control inputs, allowing it to assess the influence of these inputs on the system's state [31]. This is particularly useful in systems where control actions play a significant role in the dynamics. Traditionally, handling multiple control input points required constructing multiple DMD models and interpolating between state-transition matrices [40]. This approach can be cumbersome and computationally expensive. DMDc simplifies this process by factoring out the confounding effects of control inputs. It constructs a single model that can handle multiple control inputs, making it more efficient and easier to implement. This is achieved by augmenting the state-space representation with control inputs, allowing the model to capture the influence of these inputs on the system dynamics.

A detailed description of the DMDc model formulation is provided in *Section 2.1*, but it is important to highlight some key features beforehand. DMDc is closely related to linear state-space models and shares the primary assumption that the system is Markovian in nature. This means that the future state of the system depends only on the current state and control inputs, not on past states. Consequently, careful consideration of both spatial and temporal discretization is required in the analysis to ensure accurate modeling.

The literature on dynamic mode decomposition and its variants, such as DMDc, reveals significant advancements in data-driven modeling of complex systems [35]. DMDc offers a robust framework for incorporating control inputs and disambiguate system dynamics from actuation effects, while modal decomposition techniques like POD and Balanced POD [43] provide valuable insights into fluid flows and other high-dimensional systems. However, challenges related to noise, nonlinearity, and computational expense remain [20, 19, 44]. Future research should focus on refining these methods to enhance their robustness and applicability across various fields, ultimately improving our ability to model and understand complex systems. This study leverages DMDc to model the complex dynamics of directed energy deposition (DED) in additive manufacturing. By incorporating control inputs into the DMD framework, we aim to better understand the link between input process parameters and the final product, ultimately improving the reliability and performance of DED processes, which are significantly actuation-dependent.

2 Methods and Materials

DED is an advanced additive manufacturing process where metal powder is delivered to a substrate while a heat source, typically a laser, simultaneously induces melting, thereby depositing material layer by layer. This process allows for the precise fabrication of complex geometries and the repair of existing components. The material used in this study is Inconel 625, a nickel-based superalloy known for its high strength and resistance to oxidation and corrosion [9, 26]. The DED machine used is that of FormAlloy X1/L1, capable of providing up to 2kW of laser energy with a build volume of $250 \times 250 \times 300 \text{ mm}$ [21].

The dataset utilized in this study comprises 26 individual experiments, each designed to investigate various process parameters of the DED process using Inconel 625. The experiments were conducted under controlled conditions to ensure the reliability and reproducibility of the data. For the purpose of model training and validation, the data is split such that 25 experiments are used for training the model, and one experiment is reserved for testing. This approach ensures that the model is evaluated on unseen data, providing a robust assessment of its predictive capabilities. Data is generated during the DED process at a user-defined rate, which can range from 10 to 500 Hz, with a default rate of 100

Hz. This high-frequency data collection captures the dynamic nature of the process, providing detailed insights into the behavior of the system.

The proposed virtual test-bed workflow begins with the creation of a G-code program. G-code is the standard programming language used to control CNC machines, including those used in DED processes. It dictates the machine’s movements, laser modulation, and other critical parameters necessary for part fabrication. The G-code program is converted into a time series representation of all the inputs by the machine controller. This conversion translates the discrete commands into a continuous time series that can be analyzed and processed. The time series data undergoes a transformation where the inputs are standardized to have a zero mean and unit standard deviation. This step is crucial for ensuring that the data is on a common scale, which facilitates more effective modeling. The transformation parameters are saved for later use in inverse transformation. Although not strictly necessary, the authors have found that standardizing and normalizing the process inputs yield better results. Standardization is advantageous for mathematical reasons, primarily because it unitizes the input space, making the data more amenable to analysis and modeling.

The standardized inputs are fed into a state-space model, which iteratively predicts the observables or sensor measurements for the next time step until all inputs are processed. The state-space model is derived using DMDC, which is performed during a separate training stage of the pipeline. The predictions are then inverse transformed back into their original space, ensuring that the outputs are in the same units as the original inputs. These predictions are combined with uncertainty information to provide a comprehensive understanding of the model’s confidence in its predictions. The uncertainty information from previous builds is gathered separately with OMM data from various builds forming a cache of uncertainty information to be applied later. This cache provides valuable insights into the variability and reliability of the process, enhancing the robustness of the model’s predictions. The authors believe that this cache improves with the ingestion of more data, similar to the DMDC state-space model, thereby continuously refining the model’s accuracy and reliability. The final output of the workflow includes both a time series and a geometric digital representation of the final object. This dual output provides a detailed view of the process dynamics and the resulting part geometry.

In summary, the methods and materials described in this study provide a comprehensive framework for modeling and predicting the behavior of the DED process using Inconel 625. The integration of advanced data transformation techniques, state-space modeling, and uncertainty quantification ensures that the proposed workflow is both robust and reliable, paving the way for more effective control and optimization of additive manufacturing processes.

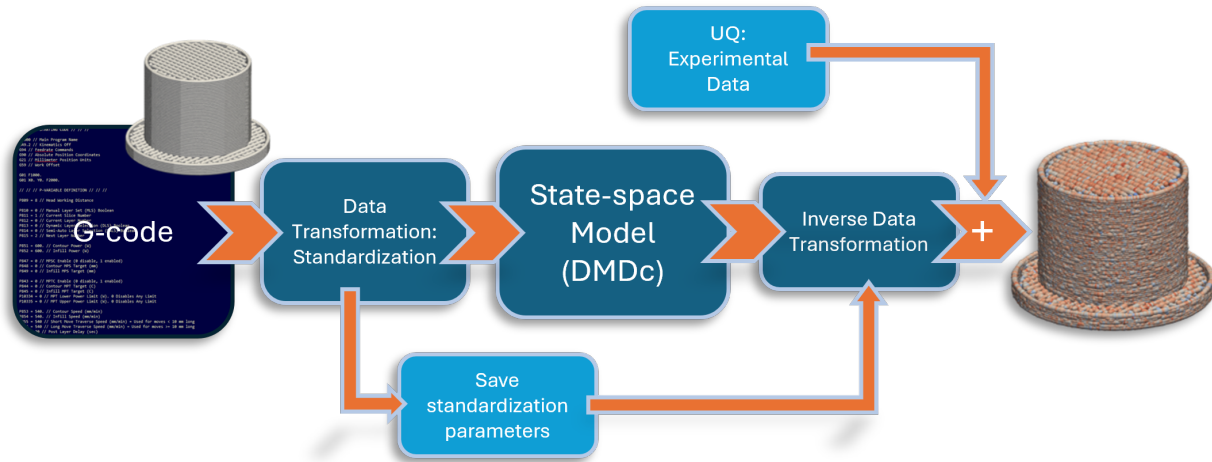


Figure 1: Chart describing the intended prediction workflow for this study and more generally the concept of a virtual test bed. G-code or time series input signals are provided, then conditioned and input into the state-space model. The state-space iteratively predicts the next time-step for the entirety of the provided input. The predictions are collected and combined with uncertainty information. The output of the workflow is both a times series and geometric digital representation of the final object.

2.1 Base Mathematical Formulation

At a fundamental level, DMD analyzes the relationship between pairs of measurements from a dynamical system. The measurements, x_t and x_{t+1} , where t denotes the temporal iteration from a discrete dynamical system, are assumed to be approximately related by a linear operator:

$$x_{t+1} \approx \mathbf{A}x_t, \quad (1)$$

where $x \in \mathbb{R}^n$ and $\mathbf{A} \in \mathbb{R}^{n \times n}$. This approximation is presumed to hold for all pairs of measurements. The subsequent discussion of DMD will focus on determining a best-fit solution for the operator \mathbf{A} across all measurement pairs. It is important to note that the relationship in Equation 1 does not need to hold exactly, as is typical with most numerical methods.

DMDc extends Equation 1 to encompass a more comprehensive state-space representation. The state-space representation of a linear dynamical system is given by:

$$\begin{aligned} x_{t+1} &= \mathbf{A}x_t + \mathbf{B}u_t \\ y_t &= \mathbf{C}x_t + \mathbf{D}u_t \end{aligned} \quad (2)$$

Assuming no direct feed-through from inputs to measurements ($\mathbf{D} = 0$) and setting \mathbf{C} to the identity matrix ($\mathbf{C} = \mathbf{I}$), we imply that there is no access to internal states ($y_t = x_t$). This assumption aligns with the data-driven hypothesis and the gappy measurement problem [17]. However, it is noteworthy that the development and previous applications of DMD utilized fluid dynamics numerical simulations where full-state access was available. The more general case described here employs measurements of a system, whether historical, numerical, or experimental, to construct the data matrix. A control-theoretic perspective would frame Equation 1 with a measurement function. A linear measurement function $x = \mathbf{C}x$ suggests an underlying system involving the variable x . In Section 8, we demonstrate how this measurement function can take different forms. Substituting into Equation 2 yields:

$$y_{t+1} = \mathbf{A}y_t + \mathbf{B}u_t \quad (3)$$

which relates the system dynamics solely as a function of input-output pairs and fits into the DMDc framework. From Equation 2, given the process inputs and recorded measurements, \mathbf{A} and \mathbf{B} are unknown, with y_t and u_t being replaced by snapshot matrices as shown in Equation 4:

$$\mathbf{Y}_t = \begin{bmatrix} | & | & & | \\ y_{t_1} & y_{t_2} & \dots & y_{t_{m-1}} \\ | & | & & | \end{bmatrix}, \mathbf{Y}_{t+1} = \begin{bmatrix} | & | & & | \\ y_{t_2} & y_{t_3} & \dots & y_{t_m} \\ | & | & & | \end{bmatrix}, \text{ and } \mathbf{U}_t = \begin{bmatrix} | & | & & | \\ u_{t_1} & u_{t_2} & \dots & u_{t_{m-1}} \\ | & | & & | \end{bmatrix} \quad (4)$$

To draw equivalence with standard DMD, Proctor *et al.* introduces two new variables, \mathbf{G} and Ω , to combine column-wise the unknowns and the measurements and process inputs (Equation 5) [31]:

$$\mathbf{Y}_{t+1} = \mathbf{G}\Omega = [A|B] \begin{bmatrix} \mathbf{Y}_t \\ - \\ \mathbf{U}_t \end{bmatrix} \quad (5)$$

$$\mathbf{G} = [A|B] = \mathbf{Y}_{t+1}\Omega^\dagger \approx \mathbf{Y}_{t+1} \times \text{SVD} \left(\begin{bmatrix} \mathbf{Y}_t \\ \mathbf{U}_t \end{bmatrix} \right)^\dagger \quad (6)$$

The \dagger symbol represents the Moore-Penrose pseudoinverse. Canonically, the singular value decomposition (SVD) uses U and V to represent the unitary matrices. However, to avoid confusion with the process input snapshot matrix \mathbf{U} , the SVD will be taken as:

$$\text{SVD}(M_{p \times q}) = \eta_{p \times r} \Sigma_{r \times r} \zeta_{r \times q}^* \quad (7)$$

Applying the SVD as previously defined to Equation 6, \mathbf{G} can be solved for both \mathbf{A} and \mathbf{B} as:

$$\begin{aligned} \mathbf{A} &= \mathbf{Y}_{t+1} \zeta \Sigma^{-1} \eta_{Y_t}^* \\ \mathbf{B} &= \mathbf{Y}_{t+1} \zeta \Sigma^{-1} \eta_{U_t}^* \end{aligned} \quad (8)$$

where $\eta_{Y_t}^*$ and $\eta_{U_t}^*$ are the measurement and process input components of the decomposition, respectively. Note that a reduced dimensionality SVD as well as projection matrices typical of DMD/DMDc are not used in this formulation. The measurement space is extremely limited (consistent with the gappy type problem), and therefore all measurements are considered linearly independent in the context of a state-space representation.

2.2 Control Theoretic Lemmas

There are two equally important aspects of the collected experimental data that contribute to the success of the DMDc representation of the true system: the density of time snapshots and the induced dynamics observed during the experiment.

The density of time snapshots is governed by the recording frequency of the data acquisition system. This frequency must be sufficient to form a compact, linear support for the underlying physical process. DMD/DMDc is a technique based on least-squares regression, and therefore, proper temporal discretization is essential for constructing an accurate model. The recording frequency essentially sets a threshold that ensures the temporal resolution is adequate to capture the dynamics of the system without aliasing. While increasing the recording frequency beyond this threshold does not necessarily improve the model, it can provide insights into measurement uncertainties and noise characteristics at the threshold frequency. For these experiments, the maximum data recording frequency is 500 Hz, with most datasets recorded at 100 Hz. This choice balances the need for high temporal resolution with practical considerations such as data storage and processing capabilities. An investigation into the optimal temporal threshold and its impact on model accuracy is provided later in Section 3, where we explore the trade-offs between recording frequency, data volume, and model fidelity.

The second crucial aspect of the collected data sets is the induced dynamics observed during the experiment. Ideally, the data set collected from a DED experiment would encompass all relevant state dynamics required to describe the system with a state-space representation. However, in the data-driven paradigm, we do not have direct access to the internal states of the system. Instead, we must approximate these state dynamics by analyzing the measurements, which are influenced by the process inputs. This approach necessitates a careful design of the experiment to ensure that the induced dynamics are sufficiently rich and informative. The measurements must capture the essential features of the system's response to various inputs, allowing for an accurate reconstruction of the underlying state-space model. These considerations have been previously formalized as the subspace identification assumptions, which have been adapted to reflect the specific challenges of our problem (see List 2.2 below) [27]. Ensuring that the induced dynamics are representative of the system's behavior under different operating conditions is critical for the success of the DMDc methodology. This involves not only selecting appropriate input signals but also ensuring that the experimental setup and data acquisition process are robust and capable of capturing the necessary dynamics.

1. $\text{rank}(y_t) = n$

The measurement vector is sufficiently excited and the system is reachable.

2. $\text{rank}(u_t) = mk$

The input sequence is persistently exciting.

3. $\text{rank}\begin{pmatrix} u_t \\ y_t \end{pmatrix} = mk + n$

y_t and u_t are not collinear, and therefore this is no "state" feedback ($u_t = \mathbf{k}y_t$).

This study examines the problem from two perspectives: inter-signal and intra-signal analysis. Inter-signal analysis, commonly referred to as feature selection in the fields of statistics, machine learning, and data science, is a critical aspect of this study [5]. The three control theoretic lemmas discussed earlier primarily fall under the umbrella of feature selection. Feature selection encompasses a set of tools and practices designed to address degeneracies in the data, thereby mitigating their adverse effects on model performance. Two prominent forms of data degeneracy are the curse of dimensionality and multicollinearity, both of which manifest similarly in regression analysis. In the limit, both the curse of dimensionality and multicollinearity tend to produce regression coefficients with little to no inter-feature sensitivity. Common techniques for addressing these issues include correlation analysis, matrix rank assessment, chi-squared tests, mutual information, recursive feature elimination, and, as utilized in this study, the variance inflation factor (VIF) method [36].

Due to the limited number of observables available, they were not subjected to any feature selection process. However, the process inputs were analyzed for multicollinearity using the VIF method. The VIF method allows for the exploration and hierarchy of inputs that produce a multicollinearity condition, whereas matrix rank assessment merely indicates the existence of such a condition. The algorithm for performing the VIF method involves selecting an individual feature and then forming a regression equation using the remaining features. The coefficients of this regression are then solved

(see Equation 9). The VIF for that feature is calculated as shown in Equation 10, where (R^2) is the coefficient of determination from the solved regression. This process is repeated for each individual feature. Empirically, VIF values greater than 10 indicate that the given feature exhibits a high degree of multicollinearity, while VIF values less than 5 suggest that the feature is independent of all other features [36]. Our feature selection algorithm involves removing features with VIF values greater than 10 and iterating through the VIF method until all features have VIF values less than 5. Additionally, we assess the traditional matrix rank at every iteration to ensure that the process is not erroneously halted.

Let, $\mathbf{U}_t^T = W$ be the feature matrix,

$$W_i = \sum_{\substack{j=1 \\ i \neq j}}^n \alpha_j W_j, \quad (9)$$

then, $\alpha_i = (W_j^T W_j)^{-1} W_j^T W_i$

$$VIF_i = \frac{1}{1 - R_i^2} \quad (10)$$

Intra-signal analysis, on the other hand, focuses on the temporal characteristics and dynamics within a single signal. This involves examining the signal's properties over time to ensure that the data accurately captures the underlying physical processes. Proper temporal discretization, as discussed earlier, is crucial for constructing an accurate model. By analyzing the intra-signal dynamics, we can identify and mitigate issues such as noise, aliasing, and other temporal artifacts that may affect the model's performance.

Intra-signal/feature analysis, often referenced in the context of techniques such as SMOTE (Synthetic Minority Over-sampling Technique) and Intelligent Feed Forward (IFF), is best understood through the lens of a classification problem [6, 10]. Consider a scenario where a single feature is categorized into six distinct classes. If there is an imbalance in the number of examples for each class, the resulting model is likely to exhibit bias. This imbalance can lead to the under-representation or even elimination of classes with fewer observations, driven by mechanisms related to the loss function or inherent uncertainty in the model. Extending this analogy to a continuous case, a balanced feature would be one that approximates a uniform distribution over its given range.

Our formulation and attempt at characterizing the "intra-feature rank" involves measuring the distance between distributions, which can be effectively accomplished using the Wasserstein distance, also known as the Earth Mover's Distance. The Wasserstein distance quantifies the amount of work required to transform one distribution into another, providing a robust metric for assessing the similarity between distributions. By employing this metric, we can rigorously evaluate the balance of a feature, ensuring that it does not introduce bias into the model due to distributional imbalances.

In summary, this study employs a comprehensive approach to data analysis, addressing both inter-signal and intra-signal aspects. The inter-signal analysis, through feature selection and multicollinearity assessment using the VIF method, ensures that the data set is robust and free from degeneracies that could impair model performance. The intra-signal analysis ensures that the temporal characteristics of the data are accurately captured, providing a solid foundation for constructing reliable and accurate models of the underlying physical processes.

2.3 Uncertainty Quantification

Uncertainty quantification (UQ) can be approached from various perspectives [37]. In the context of this study, UQ was employed to ascertain the recorded sensor noise observed in the process. The assumptions inherent to dynamic mode decomposition imply that the model is devoid of the characteristic noise inherent to the process. This study specifically aimed to determine the noise frequency and amplitude. To achieve this, the OMM data was initially segregated based on the laser state, meaning that uncertainty quantification was only performed on data collected while the laser was active. The data was then further categorized by either scan rate (mm/min) or laser pulse length (s). These quantities aim to describe transient versus steady-state process behavior through slightly different means. With a fixed recording frequency, the scan rate (mm/min) directly affects the spatial resolution that can be captured, suggesting the potential existence of a varying noise component. In contrast, laser pulse length attempts to capture the ratio of transient to steady-state processing, with short pulses having a high ratio and long pulses a low ratio, effectively capturing the tension between these states.

After appropriately filtering the data set, the objective was to ascribe both a noise frequency and amplitude to the data. Broadly, frequency was characterized by the Fast Fourier Transform (FFT) of the signal, and amplitude was quantified as a signal-to-noise ratio (SNR). Specifically, we defined the noise frequency as the largest intensity peak of the FFT

that is not the bias frequency, and the SNR as ($SNR = \mu/\sigma$). These definitions, while subject to refinement, were deemed applicable for this initial exploration.

Finally, both the noise frequency and amplitude were separately fitted to a function to facilitate the application of the UQ envelope to the DMDc state-space model output. For this purpose, a Gaussian Process (GP) model was employed due to its advantageous properties, including the provision of uncertainty bounds and ease of sampling [32]. GP models have been utilized in numerous AM related regression problems with varying levels of success, and we believe it is well-suited to the problem at hand [2, 29]. The primary drawback of GP models is their computational complexity, which is ($O(n^3)$), imposing a practical limit on the number of data points that can be fit. To address this limitation, we employed multiple GP models to form a bagging regressor. Consequently, each GP model fit a small subset of the total data, and the final function represented an aggregation of all individual GP models.

3 Results and Discussion

3.1 Process Input Analysis

An essential aspect of constructing any model is achieving a comprehensive understanding of the model's balance between interpolatory and extrapolatory behavior. Ideally, this understanding should be both qualitative and quantitative. Models that predominantly perform interpolation, as opposed to extrapolation, are generally preferred due to their increased reliability and accuracy within the range of the training data.

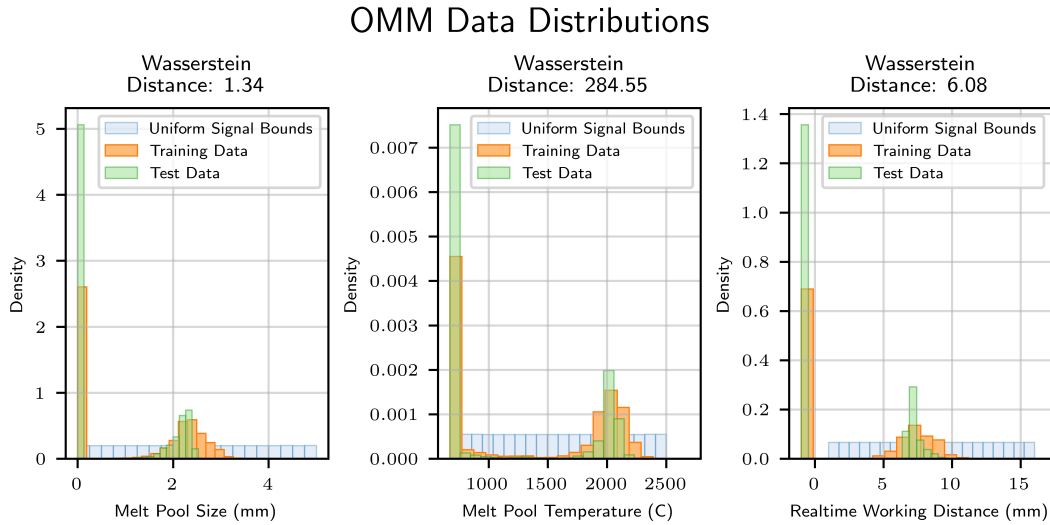


Figure 2: Distributions of DED observables versus their uniform signal bounds, the so-called "intra-feature rank." Also indicated is the Wasserstein distance for each observable.

Figure 2 illustrates the distribution of each observable (melt pool size, temperature, and working distance) compared to a uniform distribution of the same size. Above each plot, the calculated Wasserstein distance is displayed, with the minimal distance for this metric being zero. A comprehensive table, including these observables as well as all other recorded signals, is provided in the supplemental material section. From the figure, it is evident that neither the test nor the training data is sufficiently diverse to approach a uniform distribution, yet both are full rank. Notably, the distributions of the test and training data are very similar, indicating that the trained model will predominantly perform interpolation rather than extrapolation.

3.2 DMDc Solutions

The model was trained using the DMDc algorithm on roughly 1.5 million data points. The training process took 3.76 s followed by 21.96 s to reproduce the data. The test data set contained 150 thousand data points which was simulated in 2.12 s. This was performed on a PC with an 11th Gen Intel®i7 @ 3.00GHz processor and 32GB of RAM. Figures 3a and 3b show the results of the reproductive and test case respectively for a single observable. Figures containing the results from the other observables are shown in Section 8.

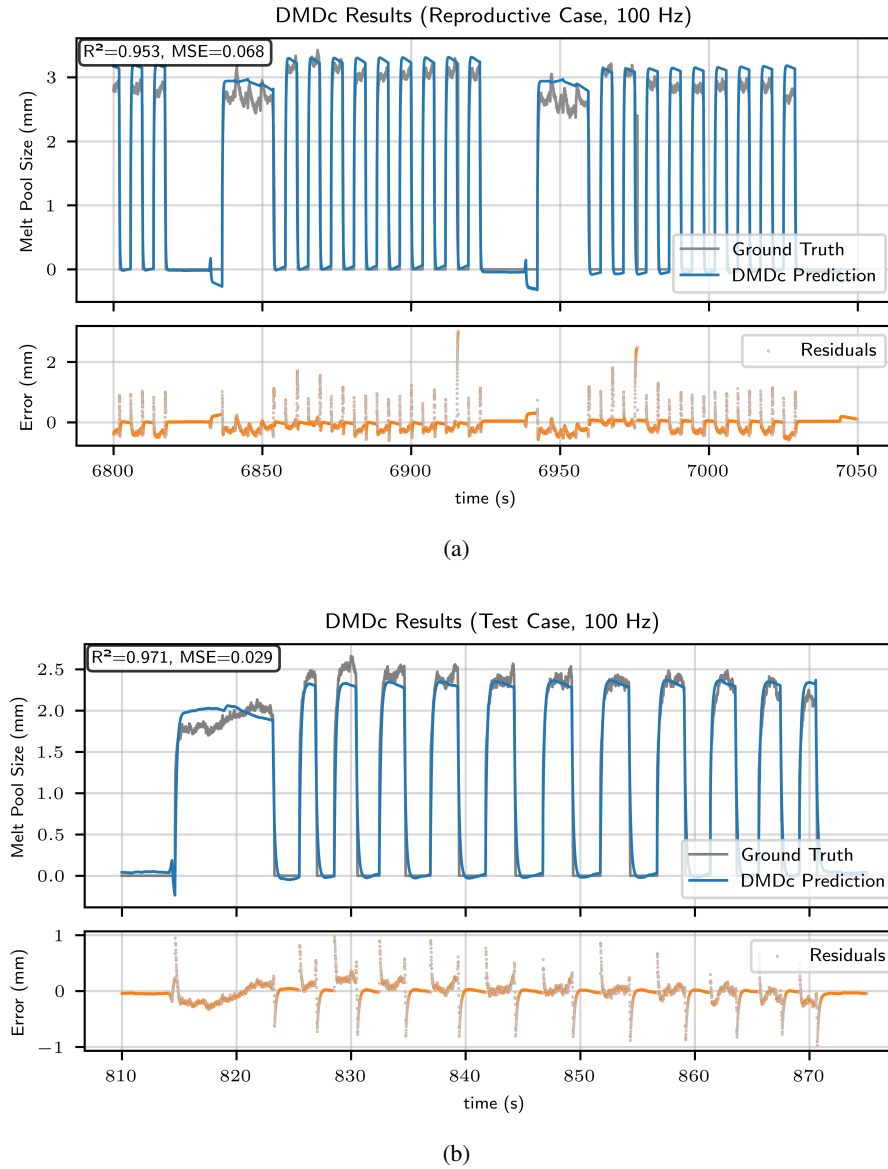


Figure 3: DMDc results for training (a) and test data (b). (top) Time series of melt pool size for both ground truth and DMDc. Inset is the R^2 and mean squared error (MSE) values of the fit. (bottom) Residuals between the experimental data and model predictions.

Though the test data performs slightly better, in R^2 and MSE , than the training data, this difference is only slight and most likely within some margin of error, so the model seems to perform as well reproducing the training data as it did on the test data. The results are very promising as the melt pool size (mm) in Figure 3b is closely matched in the test case. What is left for section 8 are the results for the other observables where melt pool temperature (C) also performs very well, but working distance (mm) only achieves an R^2 in the low 70s. This could be due to a couple of reasons: (1) the physics of working distance cannot be captured by data-driven methods, and (2) the off state, where the camera receives no input, is represented by a -1 value which could be biasing the model.

3.3 Temporal Snapshot Frequency Analysis

The experimental dataset was sub-sampled at various intervals to artificially create additional datasets at lower recording frequency. From these data sets, the entire developed DMDc pipeline was applied. The results are shown in Figure 4 with R^2 plotted as a function of hertz. With a simple spline used for illustration purposes, what is shown is the

degradation of the model accuracy as a function of the coarseness of data collection. All three sensor observables indicate a downward trend in model accuracy below a given hertz value. For melt pool temperature this occurs below 50Hz , and for both melt pool size and working distance it occurs below 20Hz . The trend holds for all sensors even when there are marked differences in the total accuracy achievable. Applying this result spatially, at relevant process speeds (upper bound of $1500\text{mm}/\text{min}$), indicates a minimum of 1 measurement every 1.25mm is required. For reference, the laser spot diameter is 1.2mm in the DED machine used for this study.

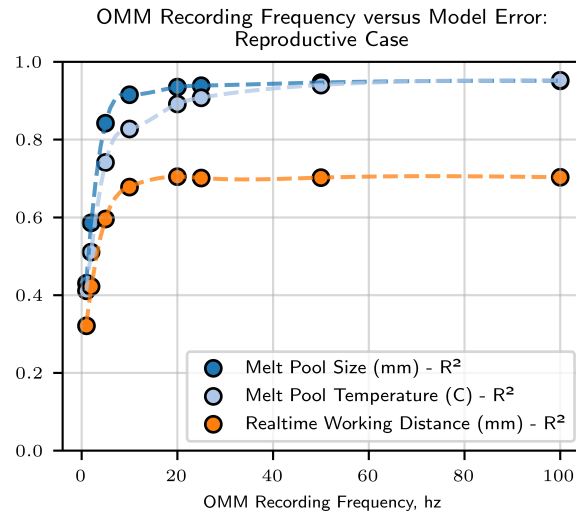


Figure 4: DMDc model error/explained variance as a response to OMM recording frequency. Melt pool temperature begins degrading below 50Hz . Melt pool size and working distance start showing significant drop off in accuracy below 20Hz .

The authors are not aware of any prior analysis in the literature that attempts to determine the minimum fidelity required for OMM data recording in DED. Most previous studies have not focused on defining the required fidelity through sensor/state observations. Instead, they have typically addressed questions such as, "What is the required sensor fidelity to detect X ?" where X often refers to porosity or other defects. In contrast, we believe we have addressed a different but equally important question: "What is the minimum sensor fidelity necessary for a dynamical system model to accurately reproduce the sensor observables?" Experimentation serves as the link between these two questions. However, our study does not attempt to describe the fidelity needed for defect detection; rather, we are prescribing a lower bound for sensor fidelity. The reality is that fidelity definitions must be established on a per-sensor and per-defect basis, while asserting that the required fidelity must exceed the previously established rates.

3.4 Experimental Data Uncertainty Quantification

Looking at the UQ results presented in *Figure 5*, which are plotted as a function of laser pulse length, we observe several intriguing findings. As anticipated, the noise frequency decreases with increasing laser pulse length across all three observables: melt pool size, working distance, and melt pool temperature. This trend aligns with our expectations, as longer laser pulses typically result in more stable and consistent measurements, thereby reducing the noise frequency.

However, the SNR trends in reveal some unexpected patterns. For both melt pool size and working distance, the SNR behaves as expected, improving with longer laser pulse lengths. This improvement indicates that the measurements become more reliable and less affected by noise. In contrast, the SNR for melt pool temperature runs counter to this trend, showing a decrease with increasing laser pulse length. This anomaly suggests that other factors might be influencing the temperature measurements, potentially related to the thermal dynamics of the melt pool or the sensitivity of the temperature sensors.

Additionally, it is noteworthy that the working distance measurement generally performs poorly. This is evident from the high uncertainty in the GP model for noise and the very low SNRs observed. The high uncertainty indicates that the model struggles to accurately predict the noise characteristics for working distance, while the low SNRs suggest that the measurements are significantly affected by noise, making them less reliable.

The results are similar when examining the UQ results plotted with respect to scan speed as shown in *Figure 6*. For working distance measurements, we again see high noise variance and low SNRs, reinforcing the challenges in obtaining accurate and reliable measurements for this observable. For both melt pool size and temperature, the noise frequency appears to remain nearly constant across the range of scan speeds, indicating that scan speed does not significantly impact the noise characteristics for these observables.

However, the SNR plots for melt pool size and temperature exhibit some unexpected behavior. Specifically, for melt pool size, there seems to be a modeling artifact that exacerbates the underlying results. This artifact could be due to limitations in the GP model or other factors not accounted for in the analysis. When examining the furthest data points at either end of the scan speed range, we observe SNRs that align in magnitude with those of melt pool temperature. This alignment suggests that, despite the modeling artifact, the overall trend in SNR for melt pool size is consistent with that of melt pool temperature, highlighting the complex interplay between scan speed, noise, and measurement reliability.

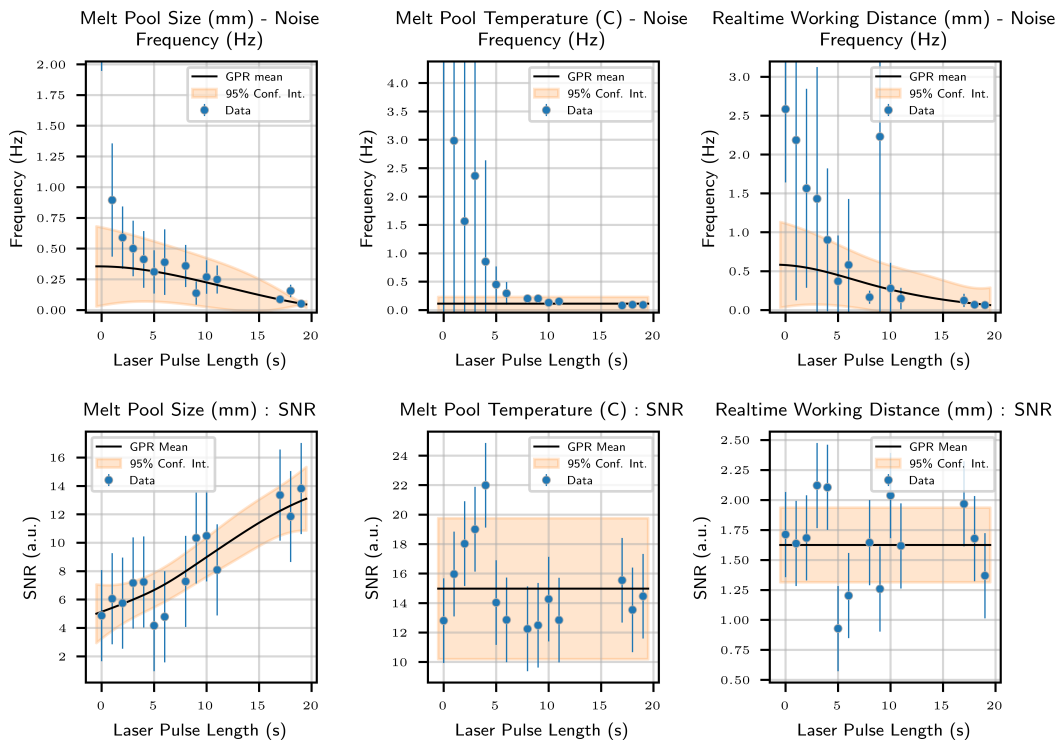


Figure 5: Noise frequency (Hz) (*top row*) and amplitude (*bottom row*) assessment on the sensor states of the experimental training data. Frequency and Signal-to-Noise Ratio (*SNR*) given as a response to laser pulse length (s)

3.5 Combined Framework Predictions

The output of this proposed framework combines the model predictions generated through the DMDc process and bounds those predictions using the UQ obtained from the experimental data. Providing expectation bounds gives machine operators real-time knowledge to understand when the process deviates from nominal conditions and requires intervention, either through parameter adjustments or by terminating the build if recovery is not feasible. These bounds also offer analysts a first-pass filtering mechanism to isolate anomalies. Linking OMM data streams to specific defects in non-single track contexts has proven challenging overall, though there have been some successes [41]. Analysis of the signal structure outside of these bounds may prove to be a viable strategy in making the problem more tractable.

The process to achieve the control plots (model predictions + UQ) shown in *Figures 7a & 7b* follows the outlined path. The model ingests process inputs of the build to be printed and yields predictions of the sensor states. These predictions are then sorted and grouped by either laser pulse length (s) or by scan rate (*mm/min*). For each grouping, a call is made to the appropriate SNR model, which produces a value. We then back-solve for the appropriate (σ),

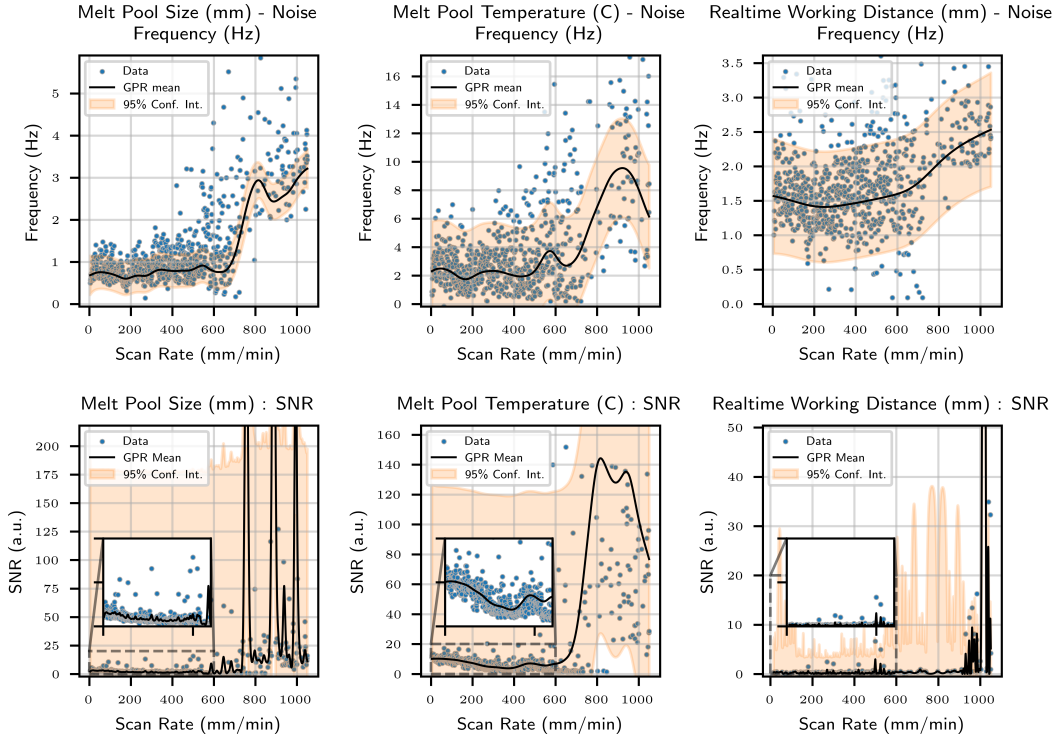


Figure 6: Noise frequency (Hz) (*top row*) and amplitude (*bottom row*) assessment on the sensor states of the experimental training data. Frequency and Signal-to-Noise Ratio (*SNR*) given as a response to scan rate (*mm/min*)

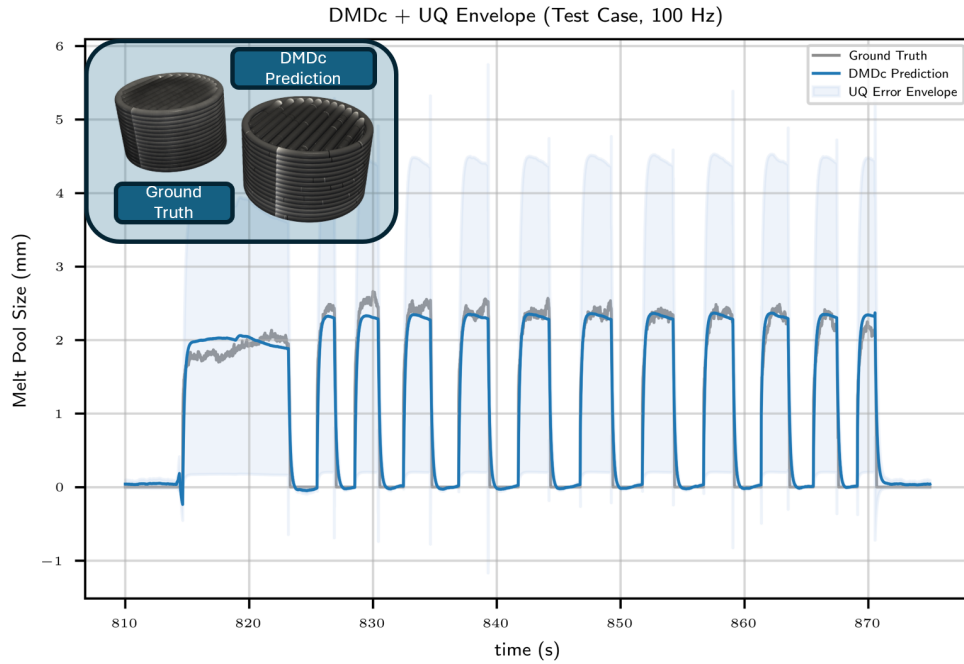
which requires an interpolation function on (μ) to account for discretization mismatch. The model prediction is then augmented by (σ) as shown in *Equation 11* to produce the bounds.

$$\begin{aligned}
 \text{Signal-to-Noise Ratio, } \text{SNR} &= \mu/\sigma, \\
 \text{rearranging for } \sigma &\text{ yields, } \sigma = \mu/\text{SNR}. \\
 \text{Now, let } \sigma^{+UQ} &= y_i^{\text{orig}}/\text{SNR}, \\
 \text{hence, } y_i^{+UQ} &= y_i^{\text{orig}} \pm \sigma^{+UQ}
 \end{aligned} \tag{11}$$

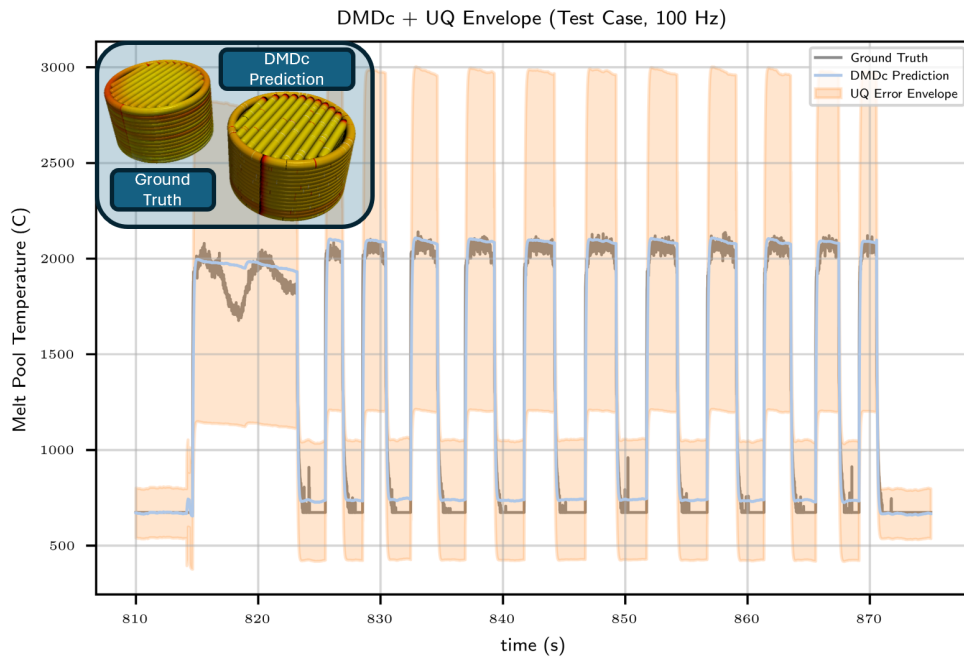
There has been no mention of incorporating the noise frequency component of the UQ analysis. Simply put, while it is important information to have—such as verifying that noise frequency does not correlate with typical electrical frequencies and their harmonics—it does not translate as well when applied to model predictions. It was attempted to sample from those points at the rate suggested by the noise frequency model and only apply the SNR to that subset of sampled points. However, beyond trying to match the experimental signal, which it doesn't do, there are no further analytical benefits to adding salt-and-pepper noise to the model predictions. It doesn't aid the operator or the analyst in the context mentioned previously. What remains to be seen is if the noise frequency model can be used to filter the experimental data rather than add the noise into the DMDC model.

Analyzing model performance through the perspective of the parity plot provides higher-level insight into the model. *Figure 8* shows such a plot for all three observables under consideration. Ignoring the -1 value in the working distance (*mm*) plot, which represents the state where the camera is making no observations, we can see that overall the model under-predicts the correct working distance. This observation correlates with the fact that the (R^2) value for this state performed significantly worse than for melt pool size or temperature. It isn't entirely clear if the inclusion of this -1 value within the experimental data set is biasing the result to cause the under-prediction. The parity plot shows that for a relatively limited experimental measurement, the model predicts a fairly large range of values.

Regarding the other two measured states, the models are performing well in terms of metrics. However, there are regions within the parity plot that show a bifurcated behavior of either under-prediction or over-prediction. The DMDC



(a)



(b)

Figure 7: Combined DMDc predictions with UQ applied as bounding envelope. Shown in (a) is melt pool size (mm) and melt pool temperature (C) in (b). Insets are 3D comparisons of the ground truth test data and the DMDc predictions.

algorithm, driven by least squares, properly balances this bifurcation, maintaining good overall quality on the metrics. Also, in those parity plots are islands with very good experimental data to prediction agreement. Continued assessment

of the bifurcated regions may indicate that the model is loosely “understanding” the physics applicable to the problem, even if only through a black-box method. The only reason to imply this is that the bifurcation regions in both the melt pool size and melt pool temperature occur around phase change areas. For melt pool temperature, the material used was Inconel 625, which has a melting temperature in the 1290 to 1350°C range [9]. For melt pool size, the laser spot diameter is 1.2mm, and therefore the concept of a melt pool doesn’t really make sense below a certain value. This could also mean that incorporating additional physics could lead to better accuracy of the model, even if a pathway to that incorporation is currently unknown.

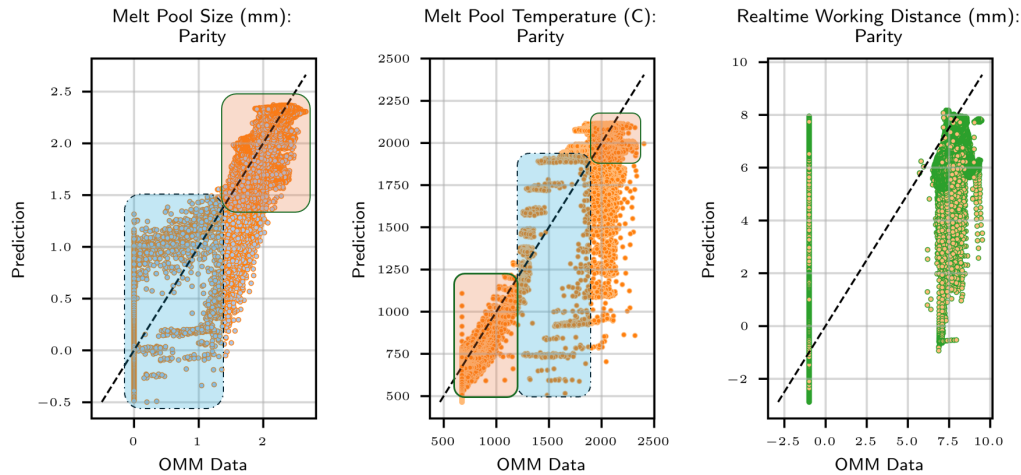


Figure 8: Parity plots for all three states measured states. Highlighted in orange are areas where the model is predicting well. Highlighted in blue are areas where the model could perform better, however, due to symmetry in the parity plot overall error remains low. Lastly, working distance (*mm*) is almost entirely under-predicted by the DMDC model

4 Conclusions

This study has presented a workflow which ingests OMM data to produce accurate sensor predictions for an unseen DED build. The model is able to produce quality predictions quickly, on the *ms* timescale. We have shown:

- The predictive power of DMDC trained on OMM data
- Produced control plots for operators and analysts using a relatively simple UQ
- Demonstrated requirements for OMM recording

To further elaborate on the above points, the success of the DMDC representation relies on two critical factors: the density of time snapshots for adequate temporal resolution and the induced dynamics that ensure the collected data effectively capture the system’s behavior. Both elements must be carefully optimized to create an accurate and reliable model of the underlying physical process. Understanding the balance between interpolatory and extrapolatory behavior is essential in model construction, and despite the training and test datasets not achieving a uniform distribution, their similarity suggests that the model will primarily perform interpolation.

The state-space model was trained using the DMDC algorithm on approximately 1.5 million data points at a rate of 2.5 μ s per data point with an inference rate of 14.35 μ s per data point on relatively standard hardware (11th Gen Intel®i7 @ 3.00GHz). Results indicate robust model performance and these findings highlight the model’s reliability while identifying areas for further refinement.

The UQ results provide insights into noise characteristics and SNR trends for different observables in DED. While some trends align with expectations, others reveal unexpected challenges, particularly in working distance measurements. The proposed framework effectively combines model predictions with UQ to offer real-time bounds, assisting operators and analysts in maintaining process control and isolating anomalies. Although the noise frequency component of UQ does not directly enhance model predictions, it has potential utility in subsequent iterations of this model and workflow. Parity plot analysis provides additional context for areas of the models strengths and weaknesses, even suggesting portions of learned physics of the system.

Additionally, the study reveals that model accuracy in this workflow unsurprisingly degrades at lower data recording frequencies, with critical thresholds identified for various sensor observables. The analysis indicates that generally a minimum of at least one measurement is required spatially at the resolution of the laser spot diameter. These authors would like to emphasize the need for establishing minimum fidelity requirements for OMM in DED, shifting the focus from defect detection to ensuring sufficient sensor fidelity for accurate dynamical system modeling.

Finally, this workflow and results also represent an important first step towards feedback control of the observables in this study. In fact, a gain operator, K_{gain} , can easily be calculated from *Equation 9* which casts the system in observable set points rather than raw process inputs, with the y_t 's coming from either previous experiments or simulated results.

$$\begin{aligned}
 y_{t+1} &= \mathbf{A}y_t + \mathbf{B}u_t \\
 \text{let } u_t &= \mathbf{K}_{gain}r_t, \text{ where } r_t \text{ is the reference input} \\
 \mathbf{K}_{gain} &= \frac{y_{t+1} - \mathbf{A}y_t}{\mathbf{B}r_t}
 \end{aligned} \tag{12}$$

5 Abbreviations

- **AM:** Additive Manufacturing
- **DED:** Directed Energy Deposition
- **DMD:** Direct Metal Deposition
- **DMD:** Dynamic Mode Decomposition
- **DMDC:** Dynamic Mode Decomposition with Control
- **ERA:** Eigensystem Realization Algorithm
- **FFT:** Fast Fourier Transform
- **GP:** Gaussian Process
- **IFF:** Intelligent Feed-Forward
- **LENS@:** Laser Engineered Net Shaping
- **LMD:** Laser Metal Deposition
- **LSTM:** Long, Short-Term Memory
- **LaSDI:** Latent Space Dynamics Identification
- **OKID:** Observer Kalman Filter Identification
- **OMM:** On-Machine Monitoring
- **POD:** Proper Orthogonal Decomposition
- **ROM:** Reduced Order Modeling
- **SINDY:** Sparse Identification of Nonlinear Dynamics
- **SMOTE:** Synthetic Minority Over-sampling Technique
- **SNR:** Signal-to-Noise Ratio
- **SVD:** Singular Value Decomposition
- **UQ:** Uncertainty Quantification
- **VIF:** Variance Inflation Factor

6 Acknowledgements

This work was performed under the auspices of the U.S. Department of Energy by Lawrence Livermore National Laboratory under Contract DE-AC52-07NA27344. This work was funded by the Laboratory Directed Research and Development Program under project tracking codes 22-SI-007 and 23-ERD-034. The LLNL document review and release number is LLNL-JRNL-865081.

7 CRediT authorship contribution statement

Michael Juhasz: Writing - original draft, Conceptualization, Investigation, Methodology, Formal Analysis. **Eric Chin:** Writing - review & editing, Conceptualization. **Youngsoo Choi:** Writing - review & editing, Conceptualization. **Joseph T. McKeown:** Writing - review & editing, Resources, Funding acquisition, Project administration. **Saad Khairallah:** Writing - review & editing, Conceptualization, Methodology, Validation, Supervision.

8 Supplemental Material

8.1 Additional Figures

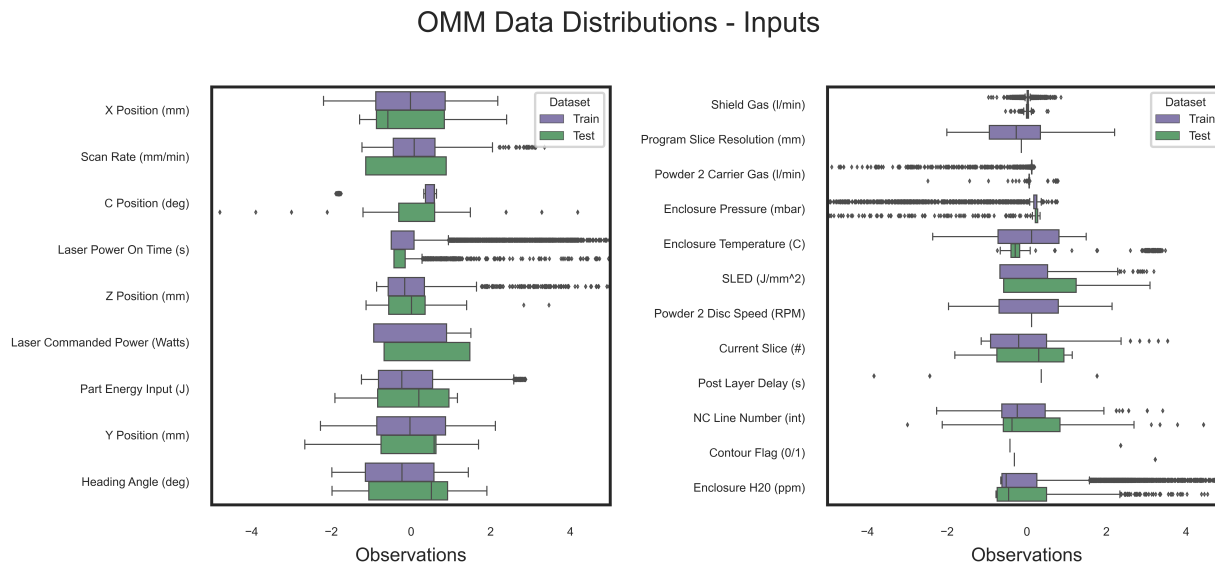


Figure S1: OMM data distributions for all other model inputs (features) in no particular order. Features are split into two separate plots and standardized for clarity. Shown are box plots comparing the training set to the test set with many features sharing distributions, however, some departures of the test set do exist.

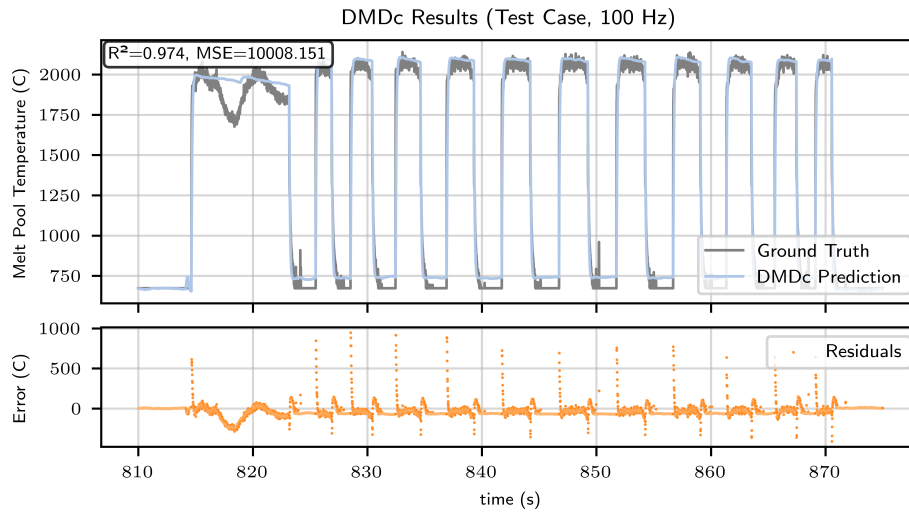
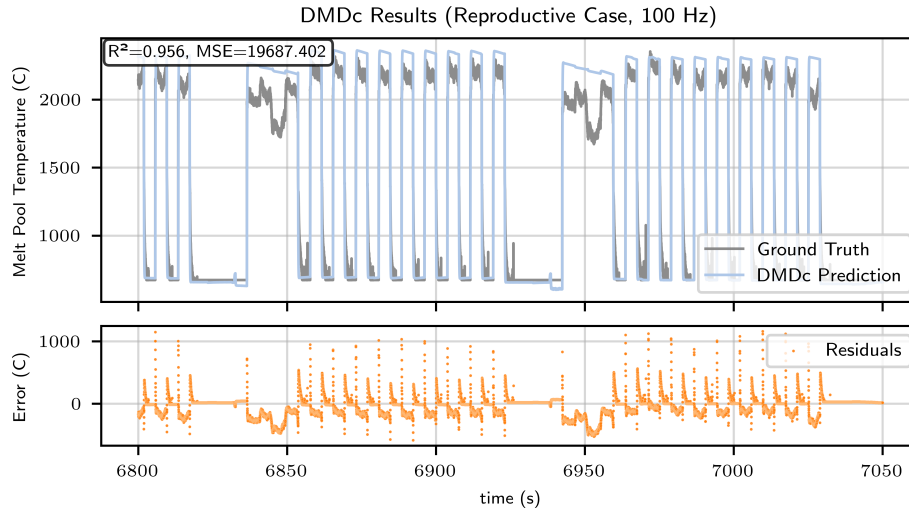
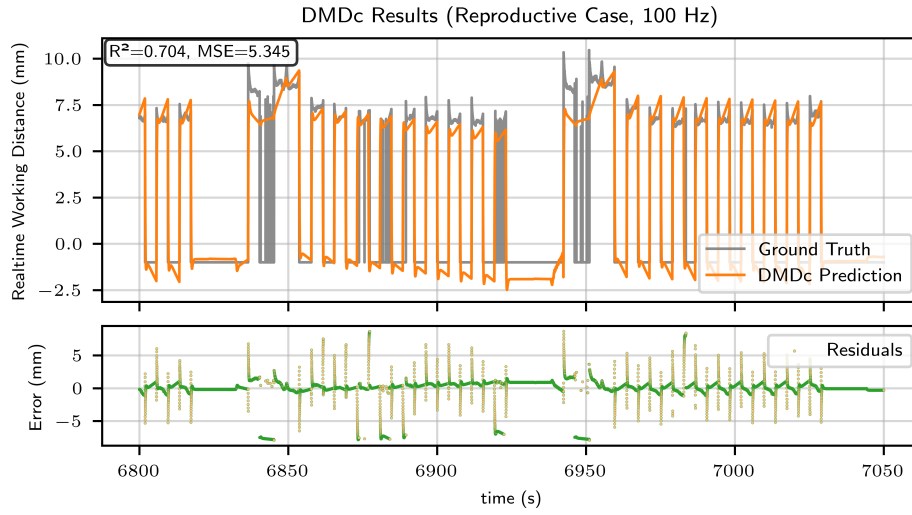
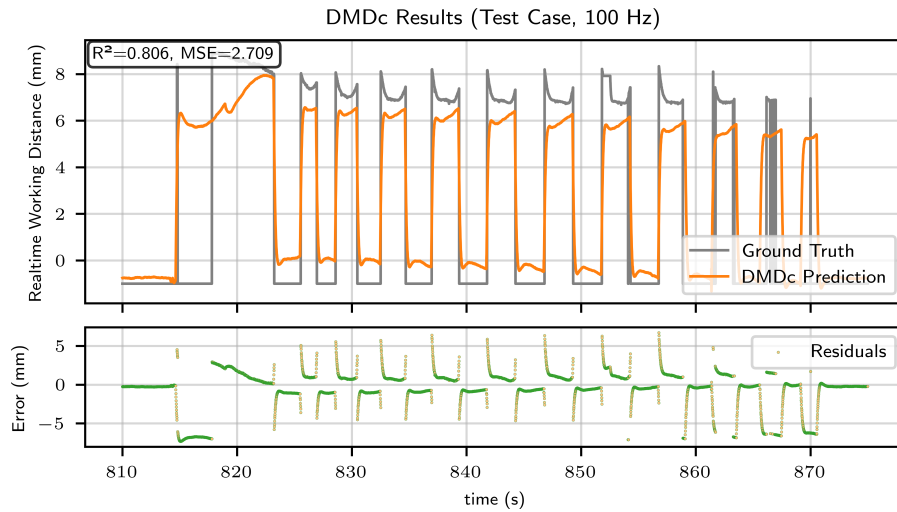


Figure S2: DMDc results for training (a) and test data (b). (top) Time series of melt pool temperature for both ground truth and DMDc. Inset is the R^2 and mean squared error (MSE) values of the fit. (bottom) Residuals between the experimental data and model predictions.



(a)



(b)

Figure S3: DMDc results for training (a) and test data (b). (top) Time series of working distance for both ground truth and DMDc. Inset is the R^2 and mean squared error (MSE) values of the fit. (bottom) Residuals between the experimental data and model predictions.

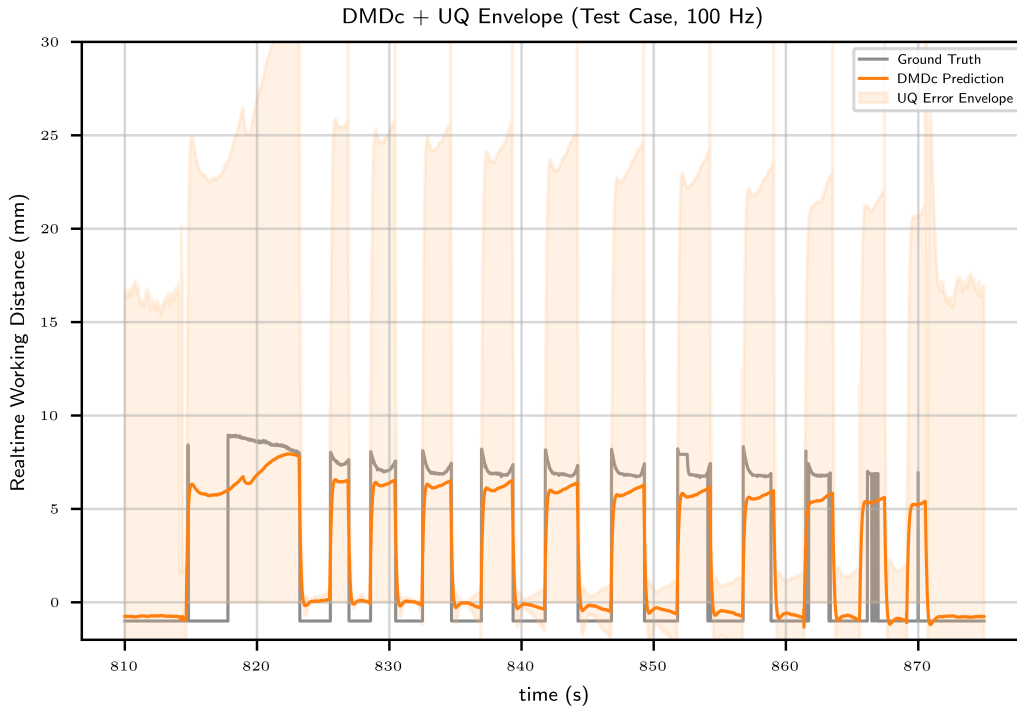


Figure S4: Combined DMDc predictions with UQ applied as bounding envelope. Shown is working distance (mm). Notice the extent of the UQ envelope demonstrating an area of needed refinement.

8.2 The dataset

The raw dataset, detailed in *section 2*, comprises 26 DED experiments involving simple square prisms, part of a process parameter development study for Inconel 625. This raw dataset consisted of 49 columns/features and 1,706,677 rows/samples. Most features are listed in *Table 1*, with some omitted due to redundancy (e.g., Powder Hopper Disc Speed 1, 2, etc.). This raw dataset was examined for missing data (NaNs) and multi-collinearity (repetitive columns). No missing data was found, but would have been removed by row/sample as part of a sound data analysis pipeline. Multi-collinearity was addressed using a feature selection algorithm based on VIF, reducing the dataset to 24 features. The test:train split for this study was 25 of those experiments for training and 1 for testing. Percentage-wise this roughly equates to a 9:91 test:train split. It is this final dataset which was used by both the DMDc algorithm and also for UQ. Notably, the dataset was not standardized before the split to avoid potential data bias.

9 References

References

- [1] D.-G. AHN, *Directed Energy Deposition (DED) Process: State of the Art*, International Journal of Precision Engineering and Manufacturing-Green Technology, 8 (2021), pp. 703–742.
- [2] F. ASADI, A. A. OLLEAK, J. YI, AND Y. GUO, *Gaussian Process (GP)-based Learning Control of Selective Laser Melting Process*, (2020).
- [3] G. BERKOOZ, P. HOLMES, AND J. L. LUMLEY, *The proper orthogonal decomposition in the analysis of turbulent flows*, Annual review of fluid mechanics, 25 (1993), pp. 539–575.
- [4] S. L. BRUNTON, J. L. PROCTOR, AND J. N. KUTZ, *Discovering governing equations from data by sparse identification of nonlinear dynamical systems*, Proceedings of the national academy of sciences, 113 (2016), pp. 3932–3937.
- [5] G. CHANDRASHEKAR AND F. SAHIN, *A survey on feature selection methods*, Computers & electrical engineering, 40 (2014), pp. 16–28.
- [6] N. V. CHAWLA, K. W. BOWYER, L. O. HALL, AND W. P. KEGELMEYER, *SMOTE: Synthetic Minority Over-sampling Technique*, Journal of Artificial Intelligence Research, 16 (2002), pp. 321–357.
- [7] A. DASS AND A. MORIDI, *State of the Art in Directed Energy Deposition: From Additive Manufacturing to Materials Design*, Coat. World, 9 (2019), p. 418.
- [8] T. DEBROY, W. ZHANG, J. TURNER, AND S. S. BABU, *Building digital twins of 3d printing machines*, Scripta Materialia, 135 (2017), pp. 119–124.
- [9] G. P. DINDA, A. K. DASGUPTA, AND J. MAZUMDER, *Laser aided direct metal deposition of Inconel 625 superalloy: Microstructural evolution and thermal stability*, Materials Science and Engineering: A, 509 (2009), pp. 98–104.
- [10] C. DRUZGALSKI, A. ASHBY, G. GUSS, W. KING, T. T. ROEHLING, AND M. J. MATTHEWS, *Process optimization of complex geometries using feed forward control for laser powder bed fusion additive manufacturing*, Additive Manufacturing, 34 (2020), p. 101169.
- [11] D. S. ERTAY, M. A. NAIEL, M. VLASEA, AND P. FIEGUTH, *Process performance evaluation and classification via in-situ melt pool monitoring in directed energy deposition*, CIRP Journal of Manufacturing Science and Technology, 35 (2021), pp. 298–314.
- [12] D. S. ERTAY, M. VLASEA, AND K. ERKORKMAZ, *Thermomechanical and geometry model for directed energy deposition with 2D/3D toolpaths*, Additive Manufacturing, 35 (2020), p. 101294.
- [13] I. O. FOR STANDARDIZATION, *Additive manufacturing — general principles — fundamentals and vocabulary (iso standard no. 52900:2021)*, (2021).
- [14] W. D. FRIES, X. HE, AND Y. CHOI, *Lasdi: Parametric latent space dynamics identification*, Computer Methods in Applied Mechanics and Engineering, 399 (2022), p. 115436.
- [15] A. GAIKWAD, R. YAVARI, M. MONTAZERI, K. COLE, L. BIAN, AND P. RAO, *Toward the digital twin of additive manufacturing: Integrating thermal simulations, sensing, and analytics to detect process faults*, IISE Transactions, 52 (2020), pp. 1204–1217. Publisher: Taylor & Francis _eprint: <https://doi.org/10.1080/24725854.2019.1701753>.
- [16] I. GOODFELLOW, Y. BENGIO, AND A. COURVILLE, *Deep learning*, MIT press, 2016.

- [17] H. GUNES, S. SIRISUP, AND G. E. KARNIADAKIS, *Gappy data: To krig or not to krig?*, Journal of Computational Physics, 212 (2006), pp. 358–382.
- [18] S. HARTMANN, O. MURUA, J. I. ARRIZUBIETA, A. LAMIKIZ, AND P. MAYR, *Digital twin of the laser-ded process based on a multiscale approach*, Simulation Modelling Practice and Theory, 132 (2024), p. 102881.
- [19] M. S. HEMATI, C. W. ROWLEY, E. A. DEEM, AND L. N. CATTAFESTA, *De-biasing the dynamic mode decomposition for applied Koopman spectral analysis of noisy datasets*, Theoretical and Computational Fluid Dynamics, 31 (2017), pp. 349–368.
- [20] M. S. HEMATI, M. O. WILLIAMS, AND C. W. ROWLEY, *Dynamic mode decomposition for large and streaming datasets*, Physics of Fluids, 26 (2014), p. 111701. Publisher: American Institute of Physics.
- [21] S. HESPELER, E. DEGHAN-NIRI, M. JUHASZ, K. LUO, AND H. S. HALLIDAY, *Deep learning for in-situ layer quality monitoring during laser-based directed energy deposition (lb-ded) additive manufacturing process*, Applied Sciences, 12 (2022), p. 8974.
- [22] J.-N. JUANG AND R. S. PAPPA, *An eigensystem realization algorithm for modal parameter identification and model reduction*, Journal of Guidance, Control, and Dynamics, 8 (1985), pp. 620–627. Publisher: American Institute of Aeronautics and Astronautics.
- [23] J.-N. JUANG, M. PHAN, L. G. HORTA, AND R. W. LONGMAN, *Identification of observer/kalman filter markov parameters-theory and experiments*, Journal of Guidance, Control, and Dynamics, 16 (1993), pp. 320–329.
- [24] M. JUHASZ, R. TIEDEMANN, G. DUMSTORFF, J. WALKER, A. D. PLESSIS, B. CONNER, W. LANG, AND E. MACDONALD, *Hybrid directed energy deposition for fabricating metal structures with embedded sensors*, Additive Manufacturing, 35 (2020), p. 101397.
- [25] S. A. KHAIRALLAH, E. B. CHIN, M. J. JUHASZ, A. L. DAYTON, A. CAPPS, P. H. TSUJI, K. M. BERTSCH, A. PERRON, S. K. MCCALL, AND J. T. MCKEOWN, *High fidelity model of directed energy deposition: Laser-powder-melt pool interaction and effect of laser beam profile on solidification microstructure*, Additive Manufacturing, 73 (2023), p. 103684.
- [26] J. J. LEWANDOWSKI AND M. SEIFI, *Metal Additive Manufacturing: A Review of Mechanical Properties*, Annu. Rev. Mater. Res., 46 (2016), pp. 151–186.
- [27] L. LJUNG, *System Identification: Theory for the User*, Pearson Education, 1998.
- [28] L. LJUNG, *Perspectives on system identification*, Annual Reviews in Control, 34 (2010), pp. 1–12.
- [29] S. MONDAL, D. GWYNN, A. RAY, AND A. BASAK, *Investigation of Melt Pool Geometry Control in Additive Manufacturing Using Hybrid Modeling*, Metals, 10 (2020), p. 683.
- [30] T. MUKHERJEE AND T. DEBROY, *A digital twin for rapid qualification of 3d printed metallic components*, Applied Materials Today, 14 (2019), pp. 59–65.
- [31] J. L. PROCTOR, S. L. BRUNTON, AND J. N. KUTZ, *Dynamic Mode Decomposition with Control*, SIAM Journal on Applied Dynamical Systems, 15 (2016), pp. 142–161. Publisher: Society for Industrial and Applied Mathematics.
- [32] C. E. RASMUSSEN, *Gaussian Processes in Machine Learning*, in Advanced Lectures on Machine Learning: ML Summer Schools 2003, Canberra, Australia, February 2 - 14, 2003, Tübingen, Germany, August 4 - 16, 2003, Revised Lectures, O. Bousquet, U. von Luxburg, and G. Rätsch, eds., Springer Berlin Heidelberg, Berlin, Heidelberg, 2004, pp. 63–71.
- [33] W. J. SAMES, F. A. LIST, S. PANNALA, R. R. DEHOFF, AND S. S. BABU, *The metallurgy and processing science of metal additive manufacturing*, Int. Mater. Rev., 61 (2016), pp. 315–360.
- [34] P. J. SCHMID, *Dynamic mode decomposition of numerical and experimental data*, Journal of Fluid Mechanics, 656 (2010), pp. 5–28.
- [35] ———, *Dynamic mode decomposition and its variants*, Annual Review of Fluid Mechanics, 54 (2022), pp. 225–254. Publisher: Annual Reviews.
- [36] N. SHRESTHA, *Detecting multicollinearity in regression analysis*, American Journal of Applied Mathematics and Statistics, 8 (2020), pp. 39–42.
- [37] T. J. SULLIVAN, *Introduction to uncertainty quantification*, vol. 63, Springer, 2015.
- [38] D. SVETLIZKY, M. DAS, B. ZHENG, A. L. VYATSKIKH, S. BOSE, A. BANDYOPADHYAY, J. M. SCHOE-NUNG, E. J. LAVERNIA, AND N. ELIAZ, *Directed energy deposition (DED) additive manufacturing: Physical characteristics, defects, challenges and applications*, Mater. Today, (2021).

- [39] H. TAHERI, M. R. B. M. SHOAIB, L. W. KOESTER, T. A. BIGELOW, P. C. COLLINS, AND L. J. BOND, *Powder-based additive manufacturing - a review of types of defects, generation mechanisms, detection, property evaluation and metrology*, International Journal of Additive and Subtractive Materials Manufacturing, (2017). Publisher: Inderscience Publishers (IEL).
- [40] J. H. TU, C. W. ROWLEY, D. M. LUCHTENBURG, S. L. BRUNTON, AND J. N. KUTZ, *On dynamic mode decomposition: Theory and applications*, Journal of Computational Dynamics, 1 (2014), pp. 391–421. Publisher: Journal of Computational Dynamics.
- [41] H. WEI, T. MUKHERJEE, W. ZHANG, J. ZUBACK, G. KNAPP, A. DE, AND T. DEBROY, *Mechanistic models for additive manufacturing of metallic components*, Progress in Materials Science, 116 (2021), p. 100703.
- [42] D. WEISZ-PATRAULT, *Fast simulation of temperature and phase transitions in directed energy deposition additive manufacturing*, Additive Manufacturing, 31 (2020), p. 100990.
- [43] K. WILLCOX AND J. PERAIRE, *Balanced model reduction via the proper orthogonal decomposition*, AIAA journal, 40 (2002), pp. 2323–2330.
- [44] H. ZHANG, C. W. ROWLEY, E. A. DEEM, AND L. N. CATTAFESTA, *Online Dynamic Mode Decomposition for Time-Varying Systems*, SIAM Journal on Applied Dynamical Systems, 18 (2019), pp. 1586–1609. Publisher: Society for Industrial and Applied Mathematics.